Two-step growth mechanism of the solid electrolyte interphase in argyrodyte/Li-metal contacts

Charity-Grace Chaney, Andrei Golov, Ambroise van Roekeghem, Javier Carrasco, Natalio Mingo

Two-step growth mechanism of the solid electrolyte interphase in argyrodyte/Li-metal contacts

Gracie Chaney,[†] Andrey Golov,[‡] Ambroise van Roekeghem,[†] Javier Carrasco,[‡,¶] and Natalio Mingo[*,†]

[†]*Universit Grenoble Alpes, CEA, LITEN, 17 rue des Martyrs, 38054 Grenoble, France*

[‡]*Centre for Cooperative Research on Alternative Energies (CIC energiGUNE), Basque Research and Technology Alliance (BRTA), Alava Technology Park, Albert Einstein 48, 01510 VitoriaGasteiz, Spain*

[¶]*Ikerbasque, Basque Foundation for Science, Plaza Euskadi 5, 48009 Bilbao, Spain*

E-mail: natalio.mingo@cea.fr

Abstract

The structure and growth of the Solid Electrolyte Interphase (SEI) region between an electrolyte and an electrode is one of the most fundamental, yet less-well understood phenomena in solid-state batteries. We present an atomistic simulation of the SEI growth for one of the currently promising solid electrolytes (Li_6PS_5Cl), based on *ab initio* trained machine learning (ML) interatomic potentials, for over 30,000 atoms during 10 ns, well-beyond the capabilities of conventional MD. This unveils a two-step growth mechanism: Li-argyrodite chemical reaction leading to the formation of an amorphous phase, followed by a kinetically slower crystallization of the reaction products into a $5Li_2SLi_3PLiCl$ solid solution. The simulation results support the recent,

experimentally founded hypothesis of an indirect pathway of electrolyte reduction. These findings shed light on the intricate processes governing SEI evolution, providing a valuable foundation for the design and optimization of next-generation solid-state batteries.

TOC graphic

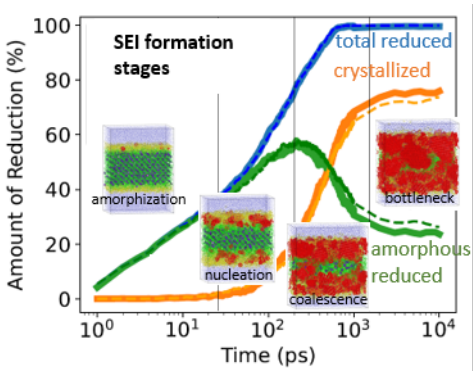

TOC graphic

Keywords

machine learning, interatomic potentials, solid-state electrolyte, battery, solid-electrolyte interphase

Introduction

Li-metal anode all-solid-state batteries (ASSBs) may replace current Li-ion batteries, since they have higher theoretical energy densities,[1,2] are potentially safer than their liquid electrolyte counterparts[3] and may also achieve longer cycling life and high power densities.[4] Sulfide argyrodite electrolytes, such as Li_6PS_5Cl (LPSC), are particularly promising for ASSB's due to their combination of high ionic conductivities and mechanical softness.[5–9] However LPSC is highly reactive when in contact with a Li-metal anode.[10] Such a system corresponds to open circuit conditions before even the first formation cycle is done. During

the reaction of LPSC with the anode, an SEI layer develops from the reduction of the thiophosphate groups. Although an SEI can hinder the rate of charge and discharge, its presence is sometimes able to protect the electrolyte from further degradation, and to increase the electrochemical stability window. This is crucial for the practical application of argyrodites in ASSB's. Understanding the physics behind the growth of the SEI in Li-metal/argyrodite contacts is therefore a priority. Experimental evidence for how this SEI forms in LPSC is however limited, and a detailed description of this process at the atomic level is currently a very sought after goal.[11,12]

Ever since the concept of SEI was proposed in 1979,[13] many modeling efforts have attempted to decipher the microscopic mechanisms behind the SEI's initial formation stages and long term growth.[14,15] Each of these models predicts different mechanisms that determine the reaction rate (ie. ionic diffusion, electron conduction, electron tunneling, vacancy diffusion, etc.) Although these different models are mutually incompatible in terms of mechanism, most of them are able to replicate the experimentally reported SEI thickness evolution. This is due to their use of adjustable parameters.(see Single *et al.*[16–18]). Thus, it is urgent to be able to perform *ab initio* simulations of SEI growth. In the specific case of solid-state electrolytes, recent progress has taken place by combining bulk *ab initio* calculations with analytical expressions and differential equations, in order to obtain the potential profile along the SEI and elucidate the main ion transport mechanisms involved in its growth.[19,20] However, fully atomistic modeling studies are still scarce. *Ab initio* molecular dynamics (AIMD) modeling has been performed.[21–24] However, AIMD is a resource-intensive method, where simulations are limited to time scales of hundreds of picoseconds, and the interface models include fewer than a thousand atoms, which seem insufficient to capture a realistic picture of the SEI growth. This problem can be circumvented by the use of *ab initio* trained machine learning interatomic potentials (MLIPs).[25–31]

Thus, the urgent need to understand the SEI growth in Li-metal/solid electrolyte contacts at the atomic level, and the limitations inherent to AIMD in previous simulations, have

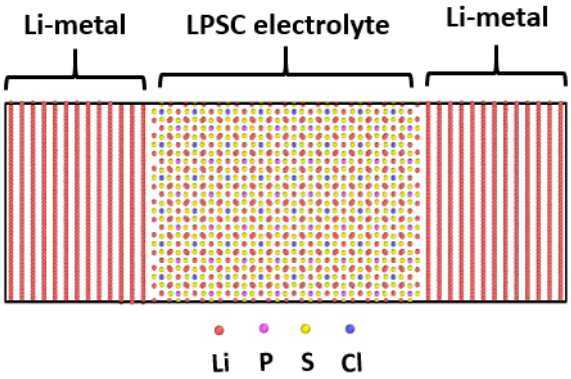

Figure 1: Li(110)/LPSC(110) interface model I.

prompted us to carry out large scale ML-MD simulations on over 30,000 atoms for tens of nanoseconds. The results unveil a rich and complex mechanism, inaccessible to shorter, smaller sized simulations. Although other phenomena are expected to happen at longer time- and length-scales, such as the coalescence and potentially the migration of the decomposed phases, we believe that our results bring new insights into the first steps of SEI nucleation. A broader analysis including mesoscopic and continuum-scale simulations could be necessary to fully understanding the growth of secondary decomposition phases.

The paragraphs below describe our use of moment tensor potentials (MTPs) with the MLIP-2 code[32] to simulate SEI formation between a Li-metal anode and an LPSC electrolyte at various temperatures, internal pressures, and initial velocities. In a 2022 paper by Wang *et al.*,[33] MTPs were also used to model the interface between Li-metal and the SEI decomposition products. As a perspective, the authors call for subsequent investigations of the formation of those products and of the full Li metal-SEI-LPSC interface, which is what we provide here. We discover a two-step growth process consisting of an initial electrolyte reduction followed by gradual crystallization of the reaction product. The value of the exponent in the crystallization's time dependence appears to be influenced by the MD temperature, suggesting a qualitative change in the driving mechanism of crystallization. Finally, we found that crystallization of the reaction product impedes the movement of Li from the anode, which can slow down the rate of further reduction. The details of our

computational methods are given in the Appendix.

Results and Discussion

We build two Li(110)/LPSC(110) interface models of different sizes following the methodology described in Ref.[21] The numbers in parentheses denote the crystallographic directions of Li and LPSC planes at the interface. Model I includes LPSC and metal Li slabs with 288 formula units and 4212 atoms, respectively (7956 atoms in total) (Fig. 1). Model II includes 1152 LPSC formula units and 16848 atoms of metal Li (31824 atoms in total). The interface surface areas of models I and II are 1345 $Å^2$ and 5380 $Å^2$, respectively. Direct visualization of the MD trajectories shows the SEI to be a mixture of amorphous and crystalline regions, the latter increasingly dominating over the former as time goes by (Figs. 2 and 3). To identify and quantify the extent of the crystalline regions, we employ a methodology developed in Ref.[34] (see below). In turn, we define the amorphous region as the part of the reduced electrolyte that is not crystalline. Fig. 2 displays the evolution of these phases over time, at three different temperatures, from two separate simulations per temperature, where the velocities at the first time step where initialized from two different random seeds (see SI). The curves in Fig. 2 clearly show the two basic steps leading to SEI growth: an initial reduction of argyrodite by metal Li results in the formation of the amorphous phase, followed by the crystallization of the reaction product. This observation is in line with the earlier hypothesis that this solid-state reduction proceeds indirectly via a metastable overlithiation, which later crystallizes in the stable products.[12,35]

As previously shown using AIMD, our results also find that the crystalline products are not a phase separated mixture of LiCl, Li_2S, and Li_3P, but a $5Li_2SLi_3PLiCl$ solid solution, which corresponds to the antifluorite structure type.[34] This is not incompatible with experimental evidence: XPS measurements have been employed to identify the three products,[11] however this experimental method, based on characterizing electronic binding energies of

individual chemical species, faces difficulties in distinguishing between phase-separated domains, or a singular solid solution, where the S sublattice comprises individual substitutions by P and Cl. Indeed, in this study part of the signal was attributed to unknown reduced P species, and the possibility of having a solid solution forming rather than separate phases for the different thermodynamically stable products has also been postulated.[35]

In terms of microstructure, the simulation allows us to identify four different reaction stages. Let's take, for example, the 400 K, 1 bar results of Figs. 2 and 3:

(1) Within the first 5 ps of the simulations, the reaction between Li and the electrolyte leads to the formation of a thin layer of amorphous product.

(2) Starting from 5 ps, the first crystalline nuclei appear in the amorphous matrix. The reaction continues with the growth of amorphous and crystalline regions. As discussed below, electrolyte conversion has a logarithmic dependence on time, while SEI crystallinity has a square root (at 300 K) or linear (at 400 K) dependence. Thus the amorphous phase dominates over the crystalline at the initial stages of the reaction.

(3) At 165 ps, electrolyte conversion reaches 71%. This point corresponds to the maximal amount of amorphous phase within reduced electrolytes. This is also when the so far separate crystalline domains start to coalesce. Subsequent growth of crystalline nuclei with a limited amount of unreacted electrolyte will lead to a decrease in the percentage of amorphous product, and a drastic slowdown in the amount of Li diffusing into the electrolyte. This slowdown might be related to the decreased Li diffusivity in the crystalline region compared to that in the amorphous one, and also to the fact that as time progresses there remains less of the original LPSC left to react with the diffusing Li.

(4) At 1 ns, all electrolyte is reduced and the crystal nuclei reach their maximum size. A further slight increase in crystallinity is due to changes in the structure of grain boundaries. We cannot expect 100% crystallinity even with longer MD simulations due to the presence of defects and grain boundaries.

Fig. 2, also shows that as temperature decreases, the system takes longer to reach its

long-term growth regime, which can be attributed to the sluggish atomic kinetics. The cases with 1 bar of internal pressure are rather similar to those with 1 kbar of internal pressure,

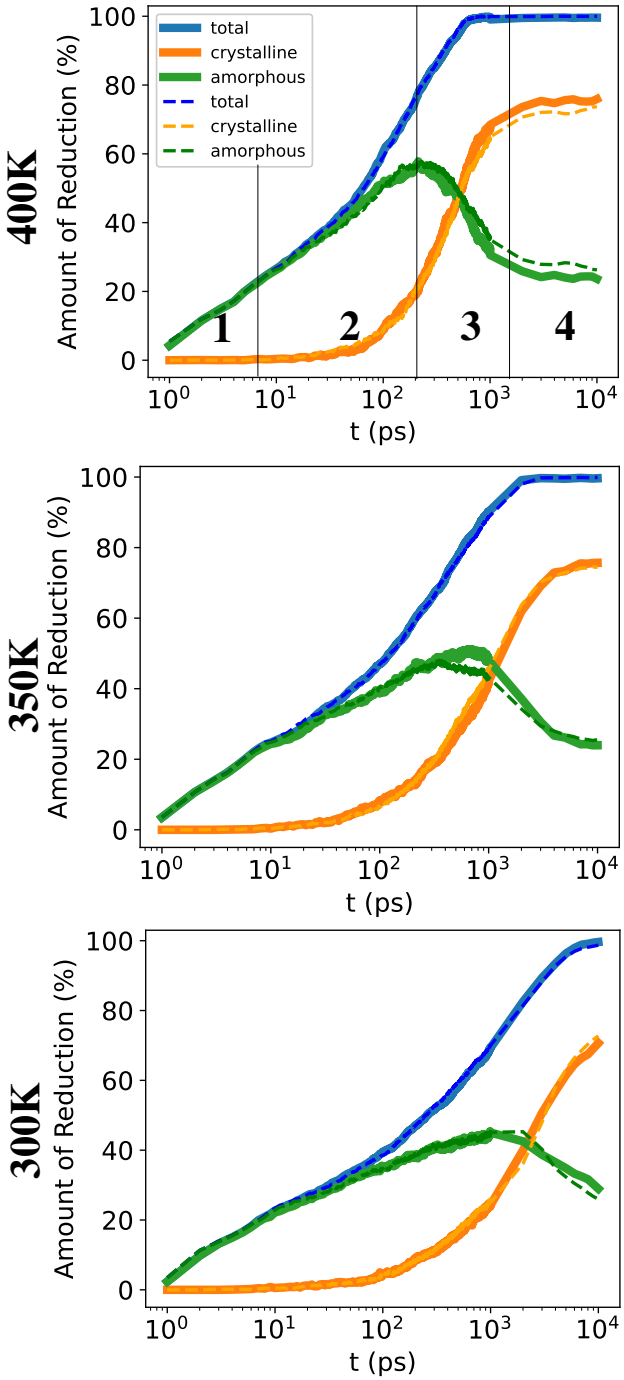

Figure 2: Percentage of reduced solid electrolyte vs time, model II. The thick and thin curves correspond to two independent MD simulations with different initial velocities.

since the fluctuations of our MD simulations are themselves over 1 kbar.

An important finding is that the amount of reduced electrolyte in the simulation increases over time t roughly as $\log(t)$ (Fig. 2). This behavior can arise if the rate of Li inflow into the electrolyte is not limited by diffusion, but by the difference in Li chemical potentials,

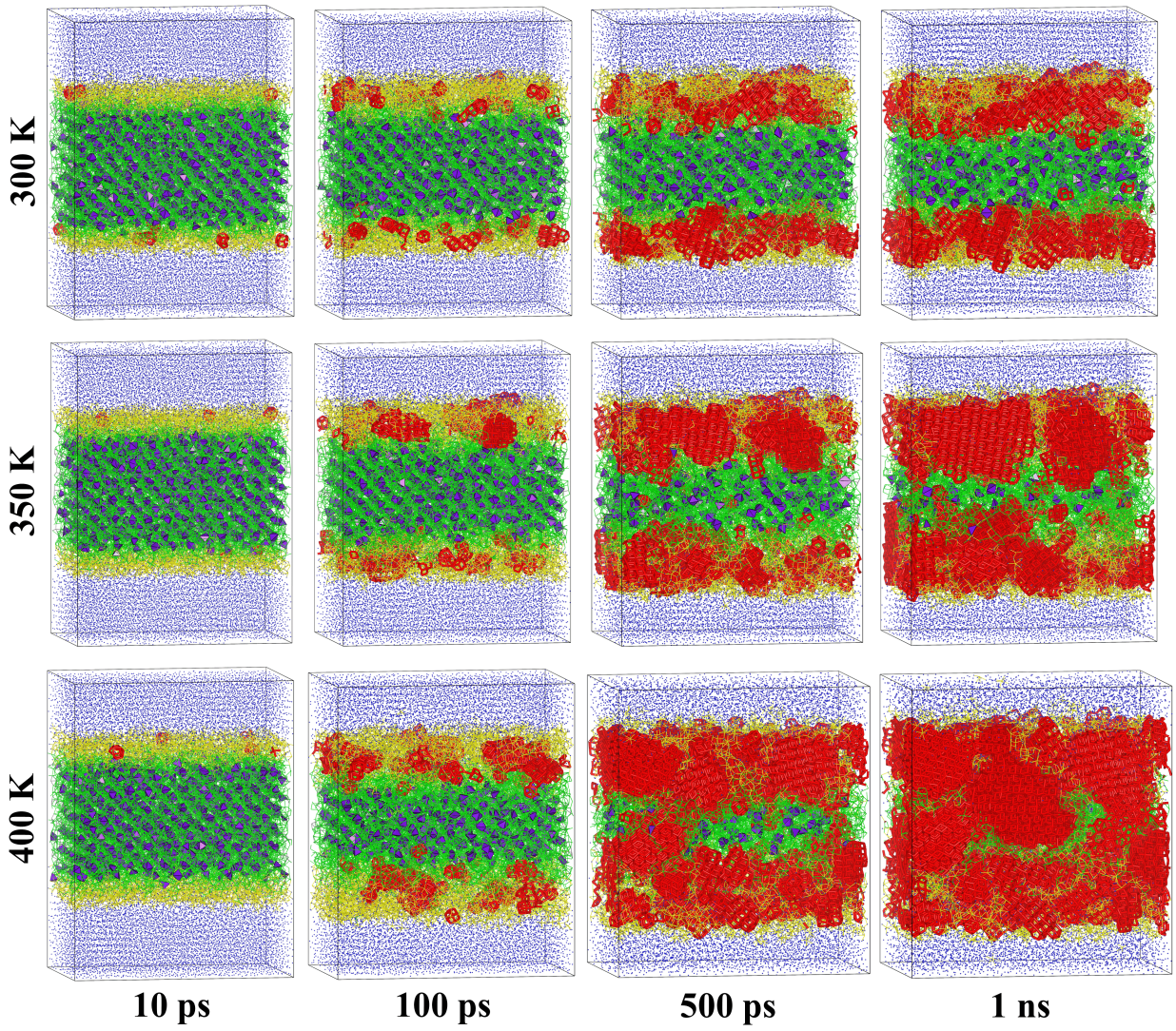

Figure 3: Evolution of the SEI. Red: crystalline regions. Yellow: amorphous reduced regions. Blue dots: Li-metal. Purple polyhedra and green lines correspond to thiophosphate groups and Li-Cl, Li-S bonds, respectively, in the original argyrodite structure. The snapshots correspond to the model II interface for various temperatures at a pressure of 1 bar (seed no. 1 for the initial velocities.) For the sake of clarity, the snapshots at 10 ns, showing full crystallization, are included in the SI rather than in this figure.

$\Delta\eta = \mu_{Li}^{A} - \mu_{Li}^{E}$ between the metal anode and the electrolyte. According to the Butler-Volmer approximation (assuming a symmetry factor $\alpha = 0.5$), $J \propto e^{\frac{\Delta\eta}{2k_BT}} - e^{-\frac{\Delta\eta}{2k_BT}}$.[36] The difference in chemical potentials progressively decreases as the electrolytes Li concentration, n, increases, and it becomes zero when the electrolyte is completely reduced, at $n = n_{\rm r}$. As a first approximation we can then write

$$\frac{1}{2}\frac{\Delta\eta}{k_BT} = \gamma(n - n_r), \tag{1}$$

which for $n << n_r$ yields

$$J \propto e^{-\gamma(n-n_{\rm r})} \equiv Ae^{-\gamma n}, \tag{2}$$

where $A = e^{\gamma n_{\rm r}}$. Since the amount of reduced electrolyte is proportional to n, we have

$$\frac{dn}{dt} = J \propto e^{-n}. \tag{3}$$

Therefore $dt \propto \frac{dn}{e^{-n}} \Rightarrow t \propto e^n$, which implies $n \propto \log(t)$.

The intuitive picture behind this logarithmic law is one where Li atoms roam unimpeded through the electrolyte, and the only limit to their flow comes from the dwindling chemical potential difference between the two reacting materials. The $\log(t)$ behavior also suggests that the electrolyte becomes reduced via a continuous lithiation process through which there is no sharp structural phase transition. It is only after being reduced, that the (by then amorphous) structure crystallizes, with an associated decrease of Li mobility. (Logarithmic growth laws are not the most common ones in physics. Another example of logarithmic behavior is the time dependence of p-MOSFET degradation, which however has a different origin.[37])

After the initial reduction of the electrolyte, crystallization occurs. The crystallization time dependence is very different from that of the amorphous reduction, and its functional

form depends on temperature (Fig. 4). For 300 K and 350 K, crystallization begins at approximately 10 ps and grows with a square-root of time dependence. Such a trend is common for diffusion-limited processes.[38–40] Above 400 K, however, crystallization acquires a linear time dependence, which is much more common for interface-limited processes.[41]

As mentioned earlier the rates of reduction and crystal growth appear to plateau in Fig. 2. It is tempting to associate this to the nearly complete reduction of the electrolyte. Nevertheless, certain simulations for the smaller system (specifically, the 1 kbar, seed 1 case of Fig. S1) show a reaction that stalls before all of the available electrolyte is reduced. This could be attributed to a negative-feedback effect in which Li-diffusion initially promotes crystallization by reducing the electrolyte, and then the growing crystals impede further Li movement within the electrolyte. Ultimately, this is because the crystalline interphase products are poor ionic conductors.[33] It appears from Fig. 3 that separate crystalline nuclei (shown in red) begin near the anode layers, before extending along all directions in three-dimensional space. Eventually, the crystal regions merge. At first, there are some pores left for the input Li to enter the electrolyte, but by 1 ns in Fig. 3, the crystal regions block nearly all incoming Li (see also section S4 of the SI).

Interestingly, the effect of different seeds on the initial velocities is marked only for the smaller systems, but becomes minor on the largest (31,824 atom) interface models. We believe this is due to the fact that crystallization proceeds akin to a percolation process. Throughout reaction stages 2, 3 and 4 (see Fig. 2), the crystalline domains start nucleating (2), coalescing (3), and finally merging into a continuous polycrystalline layer (4) that splits the electrode off the rest of the electrolyte, at which the reaction nearly stalls due to lack of Li inflow. The start of stage 4 can be viewed as the percolation threshold, at which there are no more amorphous regions left that continuously link electrode and remaining electrolyte. It is known in percolation theory that the experimental or simulated value of a system's percolation threshold becomes more reliable as the system size grows. This explains why the model I systems still present rather different electrolyte reduction and SEI crystallinity

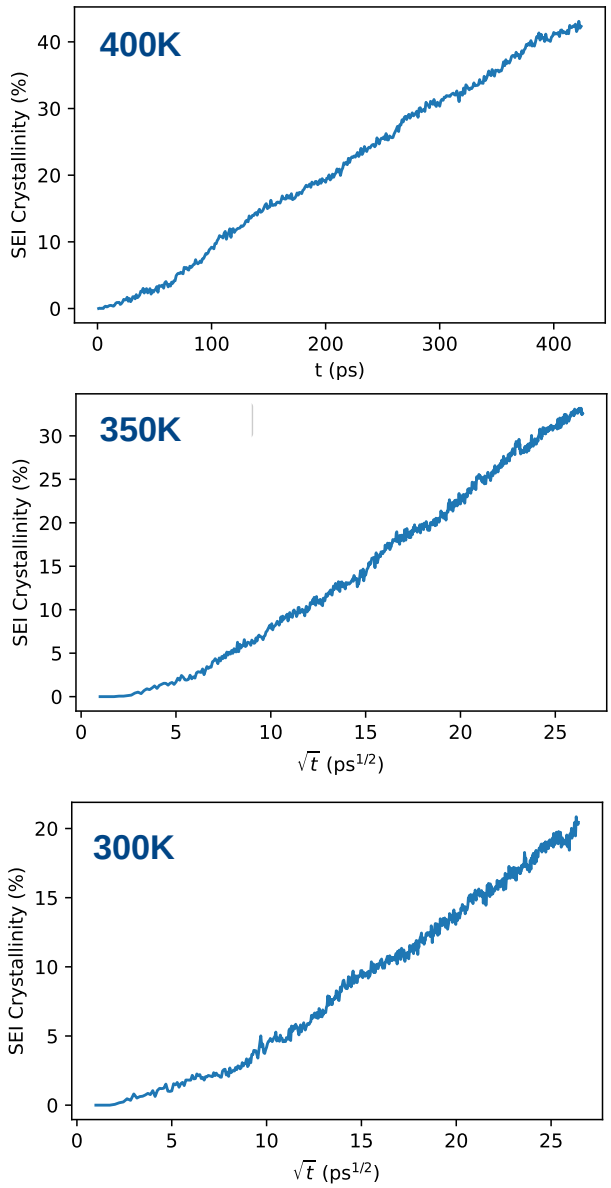

Figure 4: Amount of polycrystalline reduced electrolyte, given as a percentage of the total possible reduction, as a function of time, for the model II interface at 1 bar of internal pressure. Notice the different time scales.

curves (Fig. S1), depending on the seed, whereas the model II ones have a good match of the curves up to 10 ns (Fig. 2).

The initial stages of SEI formation just described are a fast process taking place at the timescale of nanoseconds (ns), after which the slower, long-term growth begins, limited by

the less ion-conductive $5Li_2SLi_3PLiCl$ solid solution polycrystalline layer. Directly observing the initial reaction stages poses a challenge. Perhaps nano-indentation techniques, in combination with in operando transmission electron microscopy, might enable real time imaging of the SEI time evolution at the atomistic level, in a similar way as the reorganization of metal chains during break-junction experiments was imaged some 25 years ago.[42]

The results presented are for unbiased electrolyte/electrode contacts. A welcome future development would be the ability to perform similar atomistic simulations in the presence of applied external electric fields and perhaps finite electron currents. This will require the use of new methods, including fourth-generation machine learning interatomic potentials under bias, and possibly involving non-equilibrium electron transport approaches.

Conclusion

In conclusion, we have deciphered the evolution of the atomic structure during the early stages of SEI growth at a Li-metal/LPSC interface. Machine learning-enhanced MD has enabled us to simulate systems up to 36 times larger than those previously modeled by AIMD, for trajectories up to 100 times longer.[21] This much larger timescale unveils previously unknown facts:

1) SEI formation is a two step process: Li-LPSC redox reaction leading to the formation of the amorphous phase, followed by the crystallization of the reaction products into a polycrystalline solid solution. This aligns with Schwietert *et al.'s* hypothesis of an indirect pathway.[12]

2) The redox reaction follows a logarithmic time dependence, suggesting that it is driven by a chemical potential difference. In turn, crystallization increases either linearly, or as a square-root of time, depending on temperature. This suggests interface- and diffusion-limited processes, respectively.

3) Over the 10 ns simulation we observe the onset of four distinct reaction stages: forma-

tion of the amorphous product, crystal nucleation, crystal coalescence, and reaction stalling. After the onset of the last stage, growth proceeds at orders of magnitude slower rate. The growth curves become fairly consistently reproducible, irrespective of initial velocities, when the system size exceeds 30,000 atoms.

By employing predictive atomistic simulations we can surpass inconclusive models of SEI growth based on adjustable parameters. The outcomes and insights from this study, focusing on the LPSC/Li-metal contact, serve as an illustration of the potential of this approach for various other solid electrolyte systems currently under investigation. Further developments in the field of ASSBs can highly benefit from large-scale, atomistic simulations akin to the ones showcased in this work.

Supplementary Information

In the supplementary information, we include: (1) phase evolution plots for both models of the interface, (2) active learning and cross-validation errors, (3) evidence for the diffusion bottleneck, and (4) atomic configurations of the system at 10 ns.

Acknowledgements

GC, AVR and NM thank T. Ayadi, F. Bruneval, and M. Nastar for helpful discussions. Project funded by CEA through program FOCUS-batteries. AVR and NM also acknowledge support from France 2030 through the project ANR-22-PEBA-0002.

References

(1) Wang, C.; Sun, X. The Promise of Solid-State Batteries for Safe and Reliable Energy Storage. *Engineering* **2023**, *21*, 32–35.

(2) Zhao, Q.; Stalin, S.; Zhao, C.-Z.; Archer, L. A. Designing solid-state electrolytes for safe, energy-dense batteries. *Nature Reviews Materials* **2020**, *5*, 229–252.

(3) Cheng, X.-B.; Zhao, C.-Z.; Yao, Y.-X.; Liu, H.; Zhang, Q. Recent Advances in Energy Chemistry between Solid-State Electrolyte and Safe Lithium-Metal Anodes. *Chem* **2019**, *5*, 74–96.

(4) Janek, J.; Zeier, W. G. A solid future for battery development. *Nature Energy* **2016**, *1*, 1–4.

(5) Chen, S.; Xie, D.; Liu, G.; Mwizerwa, J. P.; Zhang, Q.; Zhao, Y.; Xu, X.; Yao, X. Sulfide solid electrolytes for all-solid-state lithium batteries: Structure, conductivity, stability and application. *Energy Storage Materials* **2018**, *14*, 58–74.

(6) Park, K. H.; Bai, Q.; Kim, D. H.; Oh, D. Y.; Zhu, Y.; Mo, Y.; Jung, Y. S. Design Strategies, Practical Considerations, and New Solution Processes of Sulfide Solid Electrolytes for All-Solid-State Batteries. *Advanced Energy Materials* **2018**, *8*, 1800035.

(7) Zhang, Z.; Shao, Y.; Lotsch, B.; Hu, Y.-S.; Li, H.; Janek, J.; Nazar, L. F.; Nan, C.-W.; Maier, J.; Armand, M.; Chen, L. New horizons for inorganic solid state ion conductors. *Energy & Environmental Science* **2018**, *11*, 1945–1976.

(8) Kudu, . U.; Famprikis, T.; Fleutot, B.; Braida, M.-D.; Le Mercier, T.; Islam, M. S.; Masquelier, C. A review of structural properties and synthesis methods of solid electrolyte materials in the Li_2S P_2S_5 binary system. *Journal of Power Sources* **2018**, *407*, 31–43.

(9) Wang, Y.; Richards, W. D.; Ong, S. P.; Miara, L. J.; Kim, J. C.; Mo, Y.; Ceder, G. Design principles for solid-state lithium superionic conductors. *Nature Materials* **2015**, *14*, 1026–1031.

(10) Xiao, Y.; Wang, Y.; Bo, S.-H.; Kim, J. C.; Miara, L. J.; Ceder, G. Understanding interface stability in solid-state batteries. *Nature Reviews Materials* **2020**, *5*, 105126.

(11) Wenzel, S.; Sedlmaier, S. J.; Dietrich, C.; Zeier, W. G.; Janek, J. Interfacial reactivity and interphase growth of argyrodite solid electrolytes at lithium metal electrodes. *Solid State Ionics* **2018**, *318*, 102–112.

(12) Schwietert, T. K.; Arszelewska, V. A.; Wang, C.; Yu, C.; Vasileiadis, A.; de Klerk, N. J. J.; Hageman, J.; Hupfer, T.; Kerkamm, I.; Xu, Y.; van der Maas, E.; Kelder, E. M.; Ganapathy, S.; Wagemaker, M. Clarifying the relationship between redox activity and electrochemical stability in solid electrolytes. *Nature Materials* **2020**, *19*, 428–435.

(13) Peled, E.; Golodnitsky, D.; Ardel, G. Advanced Model for Solid Electrolyte Interphase Electrodes in Liquid and Polymer Electrolytes. *Journal of The Electrochemical Society* **1997**, *144*, L208.

(14) Yu, C.; Zhao, F.; Luo, J.; Zhang, L.; Sun, X. Recent development of lithium argyrodite solid-state electrolytes for solid-state batteries: Synthesis, structure, stability and dynamics. *Nano Energy* **2021**, *83*, 105858.

(15) Peled, E.; Menkin, S. ReviewSEI: Past, Present and Future. *Journal of The Electrochemical Society* **2017**, *164*, A1703.

(16) Single, F.; Horstmann, B.; Latz, A. Dynamics and morphology of solid electrolyte interphase (SEI). *Physical Chemistry Chemical Physics* **2016**, *18*, 17810–17814.

(17) Single, F.; Latz, A.; Horstmann, B. Identifying the Mechanism of Continued Growth of the SolidElectrolyte Interphase. *ChemSusChem* **2018**, *11*, 1950–1955.

(18) Single, F. Theory-based Investigation of the Solid Electrolyte Interphase in Lithium-ion Systems. Dissertation, Universitt Ulm, 2021.

(19) Swift, M. W.; Qi, Y. First-Principles Prediction of Potentials and Space-Charge Layers in All-Solid-State Batteries. *Physical Review Letters* **2019**, *122*, 167701.

(20) Swift, M. W.; Swift, J. W.; Qi, Y. Modeling the electrical double layer at solid-state electrochemical interfaces. *Nature Computational Science* **2021**, *1*, 212–220.

(21) Golov, A.; Carrasco, J. Molecular-Level Insight into the Interfacial Reactivity and Ionic Conductivity of a Li-Argyrodite Li_6PS_5Cl Solid Electrolyte at Bare and Coated Li-Metal Anodes. *ACS Applied Materials and Interfaces* **2021**, *13*, 4373443745.

(22) Cheng, T.; Merinov, B. V.; Morozov, S.; Goddard, W. A. Quantum Mechanics Reactive Dynamics Study of Solid Li-Electrode/Li_6PS_5Cl-Electrolyte Interface. *ACS Energy Letters* **2017**, *2*, 1454–1459.

(23) Camacho-Forero, L. E.; Balbuena, P. B. Exploring interfacial stability of solid-state electrolytes at the lithium-metal anode surface. *Journal of Power Sources* **2018**, *396*, 782–790.

(24) Wang, C.; Aoyagi, K.; Aykol, M.; Mueller, T. Ionic Conduction through Reaction Products at the ElectrolyteElectrode Interface in All-Solid-State Li+ Batteries. *ACS Applied Materials & Interfaces* **2020**, *12*, 55510–55519.

(25) Behler, J.; Parrinello, M. Generalized Neural-Network Representation of High-Dimensional Potential-Energy Surfaces. *Phys. Rev. Lett.* **2007**, *98*, 146401.

(26) Behler, J. Constructing high-dimensional neural network potentials: A tutorial review. *International Journal of Quantum Chemistry* **2015**, *115*, 1032–1050.

(27) Behler, J. Perspective: Machine learning potentials for atomistic simulations. *The Journal of Chemical Physics* **2016**, *145*, 170901.

(28) Botu, V.; Batra, R.; Chapman, J.; Ramprasad, R. Machine learning force fields: construction, validation, and outlook. *The Journal of Physical Chemistry C* **2017**, *121*, 511–522.

(29) Deringer, V. L.; Caro, M. A.; Csányi, G. Machine learning interatomic potentials as emerging tools for materials science. *Advanced Materials* **2019**, *31*, 1902765.

(30) Gokcan, H.; Isayev, O. Learning molecular potentials with neural networks. *Wiley Interdisciplinary Reviews: Computational Molecular Science* **2022**, *12*, e1564.

(31) Friederich, P.; Hse, F.; Proppe, J.; Aspuru-Guzik, A. Machine-learned potentials for next-generation matter simulations. *Nature Materials* **2021**, *20*, 750–761.

(32) Novikov, I. S.; Gubaev, K.; Podryabinkin, E. V.; Shapeev, A. V. The MLIP package: moment tensor potentials with MPI and active learning. *Machine Learning: Science and Technology* **2020**, *2*, 025002.

(33) Wang, J.; Panchal, A. A.; Sai Gautam, G.; Canepa, P. The resistive nature of decomposing interfaces of solid electrolytes with alkali metal electrodes. *J. Mater. Chem. A* **2022**, *10*, 19732–19742.

(34) Golov, A.; Carrasco, J. Unveiling Solid Electrolyte Interphase Formation at the Molecular Level: Computational Insights into Bare Li-Metal Anode and $Li_6PS_{5x}Se_xCl$ Argyrodite Solid Electrolyte. *ACS Energy Letters* **2023**, *8*, 4129–4135.

(35) Schwietert, T. K.; Vasileiadis, A.; Wagemaker, M. First-Principles Prediction of the Electrochemical Stability and Reaction Mechanisms of Solid-State Electrolytes. *JACS Au* **2021**, *1*, 1488–1496.

(36) Van der Ven, A.; Deng, Z.; Banerjee, S.; Ong, S. P. Rechargeable Alkali-Ion Battery Materials: Theory and Computation. *Chemical Reviews* **2020**, *120*, 6977–7019.

(37) Wang, Q.; Brox, M.; Krautschneider, W.; Weber, W. Explanation and model for the logarithmic time dependence of p-MOSFET degradation. *IEEE Electron Device Letters* **1991**, *12*, 218–220.

(38) Chen, Z.; Jenkins, M. J.; Hay, J. N. Annealing of poly (ethylene terephthalate). *European Polymer Journal* **2014**, *50*, 235–242.

(39) Hay, J. N. Secondary crystallization kinetics. *POLYMER CRYSTALLIZATION* **2018**, *1*, e10007.

(40) Louat, N. P. On the theory of normal grain growth. *Acta Metallurgica* **1974**, *22*, 721–724.

(41) Chason, E.; Aziz, M. J. Effect of pressure on crystallization kinetics of cordierite glass. *Journal of Non-Crystalline Solids* **1991**, *130*, 204–210.

(42) Ohnishi, H.; Kondo, Y.; Takayanagi, K. Quantized conductance through individual rows of suspended gold atoms. *Nature* **1998**, *395*, 780–783.

(43) Podryabinkin, E.; Garifullin, K.; Shapeev, A.; Novikov, I. MLIP-3: Active learning on atomic environments with Moment Tensor Potentials. 2023; `https://arxiv.org/abs/2304.13144v1`.

Appendix: Computational Methods

An overview of the training set generation, energy and force calculation, and MLIP training is given below.

Molecular Dynamics simulations

The dynamical evolution of the system is followed for 10 ns in an NPT ensemble with a Nos-Hoover thermo- and barostat. For each system, we investigated three temperatures (300 K, 350 K, and 400 K), two internal pressures (1 bar and 1 kbar), and two random seeds for initializing the velocities. We used a 1 femtosecond (fs) timestep for all systems, except for

the model II interface system at 400 K, 1 bar, seed 2, which required 0.5 fs timesteps to avoid instability.

Training Set

In general, our training set consists of structural descriptors as inputs and DFT data (energies and forces) as target values. We created our initial 2732-configuration training set, using some of the AIMD results of Golov and Carrasco's 2021 paper.[21] Using active learning, as described below, we are able to grow and refine our training set.

MLIP-2

MLIP-2 defines the local interatomic potential of an atom as a linear expansion of basis functions that are polynomial and consist of moments of inertia. These moments of inertia are the structural descriptors, consisting of radial and angular information about the local environment. A cutoff radius must be set by the user at the beginning of training to ensure smooth behavior of the radial basis functions. We chose a cutoff of 5.0 Å. It is also necessary for the user to choose the *level* of moments of the starting potential. The general rule is that a higher *level* increases the accuracy but extends the time of MLIP training. We tested a few *levels* before choosing a value of 8. We note that a newer version of MLIP has recently been released, but we did not use it in these calculations.[43]

Active Learning

Traditionally, ML models have relied on large training sets whose qualities can determine the accuracy and predictive usefulness of the model itself. Thus, a pre-step to training is often examining and refining the training data. Such a process can be tedious, time-consuming, and may even bias the data if the refining is done manually. An alternative is active learning, which is an automated process that expands the data set by selecting configurations that lead

to extrapolation. Fig 3 of Novikov's 2020 paper[32] illustrates the basic active learning process including (B) finding new structures in the training set and (D) calculating the energies and forces for the new structures. MLIP-2 determines which structures to add to the training set with the D-optimality criterion, based off of the extrapolation-grade limits, set by the user. The extrapolation-grade limits determine the ranges in which the active learning algorithm may select a non-redundant structure to add to the training-set. We gradually decrease the upper extrapolation grade from 5.5 to 2.5, while keeping the lower extrapolation grade at 1.5.

Model Accuracy

We determine when to end active learning by examining the training-set size over time. As seen in Fig. S3, the active learning algorithm stops selecting new configurations after 40 iterations. That means the configuration space has already been explored enough to achieve a reliable accuracy.

We use k-fold cross-validation to determine the accuracy of our final model on both training and test sets. Specifically, we calculate the root-mean squared absolute difference errors on 10 k-fold samples. The mean energy/atom errors are 18.36 meV/atom and 20.89 meV/atom for the training and test sets respectively.

Tracking total amount of reduction

We can track the amount of reduced electrolyte by analyzing the phosphorus coordination numbers. Throughout the reduction reaction, P atoms change their oxidation state from +5 to -3:

$\mathrm{Li_6^+P^{5+}S_5^{2-}Cl^-} + 8\mathrm{Li^0} \rightarrow 5\mathrm{Li_2^+S^{2-}} + \mathrm{Li^+Cl^-} + \mathrm{Li_3^+P^{3-}}$.

The electrolyte reduction can be viewed as a stepwise breaking of P-S bonds:

$(\mathrm{P^{5+}S_4^{2-}})^{3-} + 2\mathrm{e^-} \rightarrow (\mathrm{P^{3+}S_3^{2-}})^{3-} + \mathrm{S^{2-}}$

$(\mathrm{P^{3+}S_3^{2-}})^{3-} + 2\mathrm{e^-} \rightarrow (\mathrm{P^{+}S_2^{2-}})^{3-} + \mathrm{S^{2-}}$

$(P^{+}S_2^{2-})^{3-} + 2e^{-} \rightarrow (P^{-}S^{2-})^{3-} + S^{2-}$

$(P^{-}S^{2-})^{3-} + 2e^{-} \rightarrow P^{3-} + S^{2-}$

According to the equation, the complete reduction of one formula unit of the electrolyte requires 8 electrons. Consequently, for Z formula units, 8 Z electrons are required. At any step of molecular dynamics, the number of electrons transferred from metal Li to the electrolyte can be found from the number (N) of partially and completely reduced thiophosphate groups. Thus, the percentage of reduced argyrodite (α) can be calculated using the following formula: α =(8N(P)+6N(PS)+4N(PS_2)+2N(PS_3))/8Z

The P-S coordination numbers were calculated based on a distance criterion of 3Å.